This version of the article has been accepted for publication, after peer review (when applicable) and is subject to Springer Nature's AM terms of use (https://www.springernature.com/gp/open-research/policies/accepted-manuscript-terms), but is not the Version of Record and does not reflect post-acceptance improvements, or any corrections. The Version of Record is available online at: http://dx.doi.org/10.1038/s41586-022-04971-z

1 # Membrane-anchored HDCR nanowires drive
2 # hydrogen-powered CO_2 fixation

3
4
5

6 **Authors:**
7 Helge M. Dietrich[1†], Ricardo D. Righetto[2,3†], Anuj Kumar[1,4], Wojciech Wietrzynski[2,3],
8 Raphael Trischler[1], Sandra K. Schuller[4], Jonathan Wagner[5], Fabian M. Schwarz[1], Benjamin
9 D. Engel[2,3]*, Volker Müller[1]*, Jan M. Schuller[4]*
10

11 **Affiliations:**
12 [1] Molecular Microbiology & Bioenergetics, Institute of Molecular Biosciences,
13 Johann Wolfgang Goethe University; Frankfurt am Main, Germany
14 [2] Helmholtz Pioneer Campus, Helmholtz Munich; Neuherberg, Germany
15 [3] Biozentrum, University of Basel; Basel, Switzerland
16 [4] CryoEM of Molecular Machines, SYNMIKRO Research Center and Department of
17 Chemistry, Philipps-University, Marburg, Germany
18 [5] Department of Molecular Structural Biology, Max Planck Institute of Biochemistry;
19 Martinsried, Germany
20
21
22

23 † Equal contribution
24

25 *Correspondence to: ben.engel@unibas.ch, vmueller@bio.uni-frankfurt.de,
26 jan.schuller@synmikro.uni-marburg.de
27

Filamentous enzymes have been found in all domains of life, but the advantage of filamentation is often elusive[1]. Some anaerobic, autotrophic bacteria have an unusual filamentous enzyme for CO_2 fixation, hydrogen-dependent CO_2 reductase (HDCR)[2,3], which directly converts H_2 and CO_2 to formic acid. HDCR reduces CO_2 with higher activity than any other known biological or chemical catalyst[4,5], and therefore, it has gained considerable interest in two areas of global relevance: hydrogen storage and combating climate change by capturing atmospheric CO_2. However, the mechanistic basis of HDCR's high catalytic turnover rate remained unknown. Here, we used cryo-electron microscopy to reveal the structure of a short HDCR filament from the acetogenic bacterium *Thermoanaerobacter kivui* at 3.4 Å-resolution. The minimum repeating unit is a hexamer consisting of a formate dehydrogenase (FdhF) and two hydrogenases (HydA2) bound around a central core of one HycB3 and two HycB4. These small bacterial polyferredoxin-like proteins oligomerize via their C-terminal helices to form the backbone of the filament. By combining structure-directed mutagenesis with enzymatic analysis, we demonstrate that filamentation and rapid electron transfer through the filament enhances HDCR activity. To investigate the HDCR structure *in situ*, we imaged *T. kivui* cells with cryo-electron tomography and found that HDCR filaments bundle into large ring-shaped superstructures attached to the plasma membrane. This supramolecular organization may further enhance HDCR stability and connectivity to form a specialized metabolic subcompartment within the cell.

Main

Carbon dioxide (CO_2) is one of the primary greenhouse gases on Earth. Its continuous emission is leading to a rise in atmospheric temperature, provoking a global climate crisis that is rapidly reshaping our world[6-9] and causing massive biodiversity loss[10]. Molecular hydrogen is gaining increased attention as a means to replace fossil fuels and reduce CO_2 emissions[5,11,12]. However,

53 practical applications are limited, because H_2 has low volumetric energy density and poses an
54 explosion hazard[13]. One way to overcome these limitations is the direct hydrogenation of CO_2
55 to formic acid (HCOOH) or its conjugate base, formate ($HCOO^-$)[14-17]. Formate has an increased
56 volumetric energy density and lower combustion risk, and thus, can be utilized in sustainable
57 technologies aimed at renewable energy, hydrogen storage and CO_2 sequestration[18-21].
58 Additionally, formate is a versatile starting material for the production of higher-value carbon
59 products[22,23].

60 However, the thermodynamic stability of CO_2 makes hydrogenation a challenging reaction.
61 Almost all chemical catalysts suffer from low turnover rates or the requirement for high
62 pressure and temperature[4], making them unpractical and economically unviable. A promising
63 biocatalyst for this difficult conversion is hydrogen-dependent CO_2 reductase (HDCR), an
64 ancient enzyme that is part of the Wood-Ljungdhal pathway for CO_2 fixation in acetogenic
65 bacteria[2,3]. HDCR is the only known biological catalyst that can directly reduce CO_2 to formate
66 using H_2 as the sole electron donor. Other enzymes performing the same reaction either need
67 electrical current or soluble electron carriers as an electron source, as is the case for most
68 formate dehydrogenases, or physiologically operate in the direction of formate oxidation, as is
69 the case for formate-hydrogen lyase from *Escherichia coli*[24]. CO_2 reduction by HDCR is nearly
70 10-fold more effective than the fastest known chemical catalysts operating under harsh reaction
71 conditions (120 °C, 40 bar)[4] and over 1000-fold more effective than chemical catalysts
72 operating at comparable moderate conditions[25]. Furthermore, since the equilibrium constant is
73 close to one[26], the reaction is fully reversible under standard conditions. These superb catalytic
74 properties make HDCR a promising candidate for biotechnological applications such as
75 hydrogen production, hydrogen storage and carbon capture[27,28].

76 Like some other metabolic enzymes, HDCR forms long filaments[29], but the physiological
77 advantage of filamentation is poorly understood[1]. HDCR contains four different subunits: two

78 are small iron-sulfur proteins and two perform catalytic activities[2]. Under physiological
79 conditions, HDCR can drive reactions in both directions: it catalyzes CO_2 reduction during
80 lithotrophic growth, and it works as a formate dehydrogenase during growth on reduced C1
81 substrates such as formate or methanol[5]. H_2 oxidation and CO_2 reduction are spatially separated
82 from each other in different proteins, begging the question of how electrons manage to bridge
83 the distance between active sites.

84 To understand the molecular mechanism enabling HDCR's unsurpassed turnover rate, we used
85 single particle cryo-electron microscopy (cryo-EM) to determine the high-resolution structure
86 of HDCR filaments isolated from the thermophilic acetogenic bacterium *T. kivui*. We then
87 extended these findings from the molecular to the cellular scale by using *in situ* cryo-electron
88 tomography (cryo-ET) to visualize membrane-anchored HDCR filaments and bundles inside
89 native *T. kivui* cells.

90

91 **The Molecular Structure of HDCR**

92 HDCR was purified from *T. kivui* using a series of ion exchange and size exclusion
93 chromatography, then analyzed by cryo-EM. The micrographs were dominated by individual
94 bent short filaments (Extended Data Fig. 1). Reference-free 2D class averages revealed that
95 they consist of 3-4 repeating units. Longer filaments, similar to those previously described[29],
96 were only rarely observed (Extended Data Fig. 2A-D), likely due to fragmentation caused by
97 mechanical stress during purification and blotting onto EM grids. These longer filaments
98 formed bundles that prevented structural analysis (Extended Data Fig. 2). We acquired 33,853
99 cryo-EM images and determined the single-particle structure of a short HDCR filament with a
100 global resolution of 3.4 Å (PDB 7QV7, Fig. 1, Extended Data Table 1, Supplementary Video
101 1). In the core of the molecule, a local resolution of 2.7 Å was achieved, enabling reliable
102 modelling at the single-residue level (Extended Data Figs. 1, 3). However, the periphery only

103 reached lower resolutions (>5 Å) due to flexibility of the filament and associated enzymes.
104 Therefore, we modeled these regions with the aid of AlphaFold predictions[30] for the protein
105 backbone and homology models for cofactor positioning (Fig. 1, Extended Data Figs. 1, 3, 4,
106 5). The repeating subunit of the filament is a hexamer, with two HydA2 enzymes bound to two
107 HycB4 proteins and one FdhF enzyme bound to one HycB3. The enzymatically active proteins
108 face outwards from the HycB3-HycB4 core, forming a three-pointed star when viewed in cross
109 section (Fig. 2A).

110 HydA2 is composed of two domains, which adopt the mushroom-shaped structure of a classical
111 [FeFe] hydrogenase (Extended Data Figs. 3A, 4A). The stem domain contains two [4Fe4S]-
112 clusters that directly route electrons to the active site in the two-lobed cap domain (Fig. 2A),
113 which harbors the enzyme's catalytic H-cluster (HC). A structural superposition with the
114 closely related CpI from *Clostridium pasteurianum* (PDB 3C8Y) (Extended Data Fig. 4) shows
115 that all residues necessary for the active site are conserved[31] (Extended Data Fig. 4D). However,
116 in contrast to CpI, the accessory cluster domains 3 and 4 are missing in HydA2 (Extended Data
117 Fig. 4B), but their role is most likely substituted by the small iron-sulfur protein HycB4.

118 The FdhF density contains domains I, II and III, but in contrast to classical tungsten-dependent
119 formate dehydrogenases, domain IV is flexibly attached (Extended Data Figs. 3, 5). FdhF
120 carries a [4Fe4S]-cluster and a redox-active tungsten (Extended Data Fig. 5). The tungsten ion
121 is coordinated by the thiolate of Cys139 (see Extended Data Fig. 5, Supplementary Table 2)
122 and four dithiolene thiolates of two tungstopterin guanine dinucleotide molecules. The precise
123 catalytic mechanism of molybdenum- and tungsten-dependent formate dehydrogenases is still
124 widely debated[32-35]. However, amino acid residues reported in similar enzymes to be involved
125 in pterin-binding (see Supplementary Table 2), tungsten-ligation (Cys139) and catalysis
126 (Lys50, His140, Arg333) are highly conserved (Extended Data Fig. 5). Thus, the catalytic
127 mechanism for FdhF seems to be in accordance with previously-described enzymes of this

128 family[36]. Like other formate dehydrogenases, FdhF features a funnel-like opening that provides
129 an entry point for formate to the active site, as well as conserved residues for a putative CO_2
130 channel (Extended Data Fig. 5). Unlike other formate dehydrogenases, such as the
131 *Desulfovibrio gigas* FDH (DgW-FDH), which have a small subunit resembling bacterial
132 [4Fe4S]-ferredoxins[36], FdhF uses the structurally similar HycB3 for electron transfer (Fig. 2A).
133 Evident from the structure, a network of closely spaced (~10 Å) [4Fe4S]-clusters connects the
134 catalytic sites of FdhF and HydA2 via HycB3-HycB4 (Fig. 2A) and enables rapid electron
135 tunneling across the HDCR filament[37].

136 The small electron-conducting subunits HycB3 and HycB4 form the core of the HDCR enzyme
137 and directly connect to the enzymatic subunits. These proteins are composed of two fused
138 bacterial ferredoxin domains related by a 2-fold rotation (Fig. 2B). As in bacterial ferredoxins,
139 each domain binds to two [4Fe4S]-clusters between two α-helices on one side and a β-sheet on
140 the other side. The ferredoxin molecules are not fused sequentially, but rather, the second
141 ferredoxin-like domain is inserted into the first domain between residues 52-133 for HycB3 and
142 residues 83-165 for HycB4. HycB3 and HycB4 are very similar and superpose well, with a
143 root-mean square deviation (rmsd) of 0.96 Å. They mainly differ in loop regions that are
144 responsible for the binding specificity of the electron transferring subunit to their enzymatically
145 active counterpart. HycB4 forms a composite binding platform for HydA2, with helix ß2 and a
146 loop inserted between α2 and β3 (residues 50-67). HycB3 recruits FdhF by forming a bipartite
147 interface with helix α2 and a helical insertion between β9 and β10 (residues 99-129) of the
148 interpolated ferredoxin-like domain (Fig. 2A-B).

149 HDCR oligomerization is mediated by long C-terminal α-helices in HycB3 (residues 160-184)
150 and HycB4 (residues 190-210) (Figs. 2B, 3A). These helices are nested in a binding groove
151 formed by the β3 and β4 anti-parallel β-sheets of the respective neighboring HycB subunit. This
152 binding interface is maintained by hydrophobic interactions and H-bonds to the peptide

153 backbone. HycB4 has an additional interaction surface (Fig. 3A), a loop insertion between β9
154 and β10 (residues 135-160) that latches onto the sheets of the second ferredoxin-like domain of
155 the following HycB4 molecule in the filament. The corresponding loop in HycB3 is not
156 involved in the oligomerization interface, instead binding exclusively to FdhF. These
157 differences in the binding interfaces cause an uneven stoichiometry of HycB3-HycB4$_1$-HycB4$_2$
158 modules that form the repeating core of the HDCR filament.

159 **Filamentation Enhances HDCR Activity**

160 To address the enzymatic and physiological importance of the connectivity we observed in the
161 HDCR filament, we used plasmid-based expression (HDCR_His) to complement a *T. kivui*
162 mutant in which all the HDCR genes had been deleted (Δ*hdcr*)[38,39]. *In vivo*, HDCR_His
163 production was able to rescue the growth phenotype of the Δ*hdcr* strain (Fig. 3B). The isolated
164 HDCR_His complex had the same subunit composition as the native enzyme and also formed
165 oligomers (Extended Data Figs. 2E-F, 6, 7A-D)[3]. Due to the overproduction, the HDCR activity
166 was increased 15-fold (Extended Data Fig. 6C). We next tested whether the integrity of the
167 central filament affected enzymatic activity by producing variants devoid of either HycB3,
168 HycB4 or HydA2 (Fig. 2C, Supplementary Information File). Proteins purified with HydA2-
169 His$_6$ or His$_6$-FdhF were unable to produce formic acid from H_2 + CO_2 as well as H_2 from formic
170 acid (Fig. 2D) but retained H_2:methylviologen and formate:methylviologen oxidoreductase
171 activity, respectively (Extended Data Fig. 7E-F, Supplementary Information File).

172 To analyze the effect of filamentation on activity, we disrupted filamentation by site directed
173 mutagenesis. Our rationale for this mutation is that the C-terminal helix of HycB3 is responsible
174 for linking HDCR hexamers together and is required for filament formation, whilst the C-
175 terminal helix of HycB4 ensures integrity of the core complex itself (Figs. 2B, 3A). Indeed,
176 truncation of the HycB3 C-terminal helix (HDCR_HycB3ΔC) produced complexes with a
177 molecular mass of approximately one repeating hexameric HDCR unit, whereas

178 HDCR_HycB4ΔC complexes resembled the mass of a pair of HydA2-HycB4 dimers (Fig. 3C).
179 This interpretation is consistent with SDS-PAGE analysis of the proteins present in these
180 fractions (Fig. 3D). The C-terminal truncations had no detrimental effect on H_2:methylviologen
181 and formate:methylviologen activity (Extended Data Fig. 7E-F), but formate production from
182 H_2 + CO_2 was reduced substantially (Fig. 3E, Extended Data Fig. 7G-H). Single hexameric
183 HDCR units (HDCR_HycB3ΔC) performed formate conversion to H_2 with 18 % and formate
184 production from H_2 + CO_2 with 33 % of the original filamentous HDCR activity, whereas
185 disruption of the subunit connection within the HDCR hexamer (HDCR_ HycB4ΔC) caused a
186 complete loss of HDCR activity. This is further corroborated by deletion of the iron-sulfur
187 cluster HycB4 [4Fe4S] IV. This cluster is not required for direct electron transfer between
188 neighboring enzymes pairing with HycB3 and $HycB4_1$[37], but it is required for forwarding
189 electrons from $HycB4_1$ to $HycB4_2$ or from HycB3 to $HycB4_2$ of the adjacent HDCR unit to
190 reach additional catalytic sites (Fig. 4A-B). As a consequence of the HDCR_HycB4Δ[4Fe4S]
191 IV mutation, electrons from formate oxidation can only be shuttled directly to the closest
192 hydrogenase, and indeed, activity was only 6 % for H_2 evolution from formate and only 12 %
193 for formate production from H_2 + CO_2 (Fig. 3E). Furthermore, wild-type HDCR shows
194 variations in filament size[29], enabling us to check the filamentation-activity relationship without
195 mutagenesis. When we separated HDCR_His by gel filtration, there was a clear correlation
196 between filament size and activity, which decreased from 100 % to 50 % and 32 % (Fig. 3F).

197 Impairing filament formation and electron transfer not only reduced HDCR activity *in vitro* but
198 also *in vivo*. The HDCR_HycB3ΔC and HDCR_HycB4Δ[4Fe4S] IV mutants partially rescued
199 the Δ*hdcr* strain phenotype but showed greatly impaired growth (doubling time 4.4 h) compared

200 to wild-type (2.4 h) and HDCR_His complementation strains (2.6 h), even with glucose as
201 growth substrate and electron donor for HDCR (Fig. 3B).

202 In summary, the filamentous form of HDCR is the most active state of the enzyme. Whereas a
203 conductive connection between four adjacent subunits is sufficient for low HDCR activity
204 (HDCR_HycB4Δ[4Fe4S] IV, 72 U/mg for H_2 evolution and 97 U/mg for formate production),
205 increasing filament length as well as the number of connected subunits and therefore providing
206 additional active sites steadily enhances catalytic activity (HDCR_ HycB3ΔC, two hydrogenase
207 subunits, 234 U/mg H_2 evolution and 277 U/mg formate production) and leads to the unrivalled
208 turnover rates of filamentous HDCR (1273 U/mg H_2 evolution and 826 U/mg formate
209 production). Besides the improved connectivity of the filament, the additional protein-protein
210 interactions in the filament likely stabilize attachment of the peripherally-associated enzymes.
211 In particular, the HycB3-FdhF subcomplex would have a very exposed position in the minimal
212 repeating unit. Additionally, filament formation likely rigidifies the HycB backbone, locking
213 this central nanowire in a conformation that is favorable for efficient electron transport, with
214 constant distances between [4Fe4S] clusters. This may allow electrons to be transported over
215 long distances to reduce a CO_2 molecule far from the H_2 oxidation site (Fig. 4C-D). The HDCR
216 nanowire might store electrons, as previously described for non-enzymatic multicytochrome
217 and multiheme proteins[40-42], allowing a spatial and temporal separation of the two reactions that
218 helps maximize enzymatic activity. To the best of our knowledge, HDCR is the first example
219 of multiple enzymes connected by an electron nanowire, a molecular architecture that has great
220 potential for biotechnology applications.

221 **Cellular architecture of HDCR filaments**

222 To investigate the *in vivo* relevance of HDCR filaments, we vitrified *T. kivui* cells onto EM
223 grids, thinned them with a focused ion beam[43], then imaged their native cellular interiors in 3D
224 by *in situ* cryo-ET[44,45]. In the majority of wild-type tomograms, we observed bundles of

225 filaments attached to the plasma membrane (Fig. 5A-F, Extended Data Fig. 8A-F,
226 Supplementary Video 2). The complete absence of these filaments in the *T. kivui* Δ*hdcr* strain
227 confirmed that they are indeed HDCR (Extended Data Fig. 8G-L). Subtomogram averaging
228 revealed the molecular architecture of the HDCR bundles, resolving the native filament
229 structure at 17 Å (Fig. 5G-I, Extended Data Fig. 9). By mapping these averages back into the
230 cellular volumes, we discovered that the bundled filaments assemble into large ring-shaped
231 superstructures attached to the plasma membrane (Fig. 5C-F). We observed both partial and
232 complete rings, the latter of which were built from ~100 filaments and spanned ~200 nm inner
233 diameter.

234 We noted two differences between the structure of isolated HDCR (Figs. 1-4) and the average
235 of HDCR within the cell (Fig. 5). First, the native cryo-ET structure has a larger helical pitch
236 (Extended Data Fig. 9C), which might be enforced by lateral interactions within the bundle
237 (Fig. 5A inset, G). The isolated filament fragments in the single particle cryo-EM structure have
238 been removed from these interactions, and thus may twist into a more relaxed conformation,
239 decreasing the helical pitch. Second, while the central HycB3-HycB4 electron wire fits well
240 into the density of the cryo-ET average (Fig. 5H), the peripheral densities corresponding to
241 HydA2 and FdhF were present but not as well resolved (Fig. 5I). This could be due to variable
242 pitch between different bundled filaments, which would blur peripheral densities in the average,
243 or alternatively, it could indicate non-stoichiometric occupancy of HydA2 and FdhF along the
244 filaments. The latter idea is consistent with the stoichiometries of HydA2:FdhF in high-
245 molecular mass fractions of filamentous HDCR (Fig. 3C-D), which differ from the 2:1 ratio
246 seen in our cryo-EM structure of a completely occupied filament fragment. If the central regions
247 of the bundles consist of electron wires without enzymes, this would mean that the isolated
248 fragments in the cryo-EM structure originate mostly from the peripheral regions of the bundles,
249 which presumably would have higher HydA2 and FdhF occupancy. Variable occupancy of
250 enzymes (electron sources and sinks) along bundled HDCR filaments could have implications

251 for electron flow within the ring-shaped superstructures. Lateral conductivity between bundled
252 filaments might also be possible in regions of low enzyme occupancy.

253 The functional consequences of HDCR bundling and membrane connection remain areas for
254 future investigation. This could serve a structural role, helping to stabilize filaments and maybe
255 facilitating nucleation of new filaments. Many acetogenic bacteria live in extreme, energy-
256 limited environments that demand efficient capture of rare gaseous substrates such as H_2 and
257 CO_2[46,47]. Perhaps the molecular connectivity and supramolecular architecture of HDCR help
258 coordinate a hydrogen- and carbon-concentrating mechanism, enabling metabolism close to the
259 thermodynamic limit of life[46].

260 The unsurpassed catalytic activity of HDCR makes it a promising tool for H_2 storage and carbon
261 capture[5,20,48-50], reactions that underly the production of renewable fuels and potentially even
262 the development of negative emission technologies to combat climate change. Our study reveals
263 the exquisite connectivity of HDCR filaments and bundles, providing a molecular blueprint for
264 future bioengineering applications.

265

266 **References**

267 1 Park, C. K. & Horton, N. C. Structures, functions, and mechanisms of filament forming
268 enzymes: a renaissance of enzyme filamentation. *Biophys. Rev.* **11**, 927-994 (2019).

269 2 Schuchmann, K. & Müller, V. Direct and reversible hydrogenation of CO_2 to formate
270 by a bacterial carbon dioxide reductase. *Science* **342**, 1382-1385 (2013).

271 3 Schwarz, F. M., Schuchmann, K. & Müller, V. Hydrogenation of CO_2 at ambient
272 pressure catalyzed by a highly active thermostable biocatalyst. *Biotechnol. Biofuels* **11**,
273 237 (2018).

274 4 Sordakis, K. *et al.* Homogeneous Catalysis for Sustainable Hydrogen Storage in Formic
275 Acid and Alcohols. *Chem. Rev.* **118**, 372-433 (2018).

276 5 Müller, V. New Horizons in Acetogenic Conversion of One-Carbon Substrates and
277 Biological Hydrogen Storage. *Trends Biotechnol.* **37**, 1344-1354 (2019).
278 6 Scheffers, B. R. *et al.* The broad footprint of climate change from genes to biomes to
279 people. *Science* **354**, aaf7671 (2016).
280 7 Pecl, G. T. *et al.* Biodiversity redistribution under climate change: Impacts on
281 ecosystems and human well-being. *Science* **355**, eaai9214 (2017).
282 8 DeWeerdt, S. Sea change. *Nature* **550**, S54-S58 (2017).
283 9 Masson-Delmotte, V. *et al.* IPCC, 2021: *Climate Change 2021: The Physical Science*
284 *Basis. Contribution of Working Group I to the Sixth Assessment Report of the*
285 *Intergovernmental Panel on Climate Change.* (Geneva, Switzerland, 2021).
286 10 Ripple, W. J. *et al.* World Scientists' Warning to Humanity: A Second Notice.
287 *Bioscience* **67**, 1026-1028 (2017).
288 11 Rand, D. A. J. & Dell, R. M. *Hydrogen Energy: Challenges and Prospects*. (Royal
289 Society of Chemistry, Cambridge, 2007).
290 12 Chu, S. & Majumdar, A. Opportunities and challenges for a sustainable energy future.
291 *Nature* **488**, 294-303 (2012).
292 13 Fukuzumi, S. Bioinspired Energy Conversion Systems for Hydrogen Production and
293 Storage. *Eur. J. Inorg. Chem.* **2008**, 1351-1362 (2008).
294 14 Joo, F. Breakthroughs in hydrogen storage--formic Acid as a sustainable storage
295 material for hydrogen. *ChemSusChem* **1**, 805-808 (2008).
296 15 Loges, B., Boddien, A., Gärtner, F., Junge, H. & Beller, M. Catalytic Generation of
297 Hydrogen from Formic acid and its Derivatives: Useful Hydrogen Storage Materials.
298 *Top. Catal.* **53**, 902-914 (2010).
299 16 Mellmann, D., Sponholz, P., Junge, H. & Beller, M. Formic acid as a hydrogen storage
300 material - development of homogeneous catalysts for selective hydrogen release. *Chem.*
301 *Soc. Rev.* **45**, 3954-3988 (2016).

302 17 Eppinger, J. & Huang, K.-W. Formic Acid as a Hydrogen Energy Carrier. *ACS Energy*
303 *Lett.* **2**, 188-195 (2016).
304 18 Enthaler, S., von Langermann, J. & Schmidt, T. Carbon dioxide and formic acid—the
305 couple for environmental-friendly hydrogen storage? *Energy Environ. Sci.* **3**, 1207-
306 1217 (2010).
307 19 Agarwal, A. S., Zhai, Y., Hill, D. & Sridhar, N. The Electrochemical Reduction of
308 Carbon Dioxide to Formate/Formic Acid: Engineering and Economic Feasibility.
309 *ChemSusChem* **4**, 1301-1310 (2011).
310 20 Pereira, I. A. An Enzymatic Route to H_2 Storage. *Science* **342**, 1329-1330 (2013).
311 21 Preuster, P., Papp, C. & Wasserscheid, P. Liquid Organic Hydrogen Carriers (LOHCs):
312 Toward a Hydrogen-free Hydrogen Economy. *Acc. Chem. Res.* **50**, 74-85 (2017).
313 22 Li, H. *et al.* Integrated electromicrobial conversion of CO_2 to higher alcohols. *Science*
314 **335**, 1596 (2012).
315 23 Yishai, O., Lindner, S. N., Gonzalez de la Cruz, J., Tenenboim, H. & Bar-Even, A. The
316 formate bio-economy. *Curr. Opin. Chem. Biol.* **35**, 1-9 (2016).
317 24 Pinske, C. & Sargent, F. Exploring the directionality of *Escherichia coli* formate
318 hydrogenlyase: a membrane-bound enzyme capable of fixing carbon dioxide to organic
319 acid. *MicrobiologyOpen* **5**, 721-737 (2016).
320 25 Wang, W. H., Himeda, Y., Muckerman, J. T., Manbeck, G. F. & Fujita, E. CO_2
321 Hydrogenation to Formate and Methanol as an Alternative to Photo- and
322 Electrochemical CO_2 Reduction. *Chem. Rev.* **115**, 12936-12973 (2015).
323 26 Matubayasi, N. & Nakahara, M. Hydrothermal reactions of formaldehyde and formic
324 acid: free-energy analysis of equilibrium. *J. Chem. Phys.* **122**, 074509 (2005).
325 27 Kottenhahn, P., Schuchmann, K. & Müller, V. Efficient whole cell biocatalyst for
326 formate-based hydrogen production. *Biotechnol. Biofuels* **11**, 93 (2018).

327 28 Schwarz, F. M. & Müller, V. Whole-cell biocatalysis for hydrogen storage and syngas
328 conversion to formate using a thermophilic acetogen. *Biotechnol. Biofuels* **13**, 32
329 (2020).
330 29 Schuchmann, K., Vonck, J. & Müller, V. A bacterial hydrogen-dependent CO_2
331 reductase forms filamentous structures. *FEBS J.* **283**, 1311-1322 (2016).
332 30 Jumper, J. *et al.* Highly accurate protein structure prediction with AlphaFold. *Nature*
333 **596**, 583-589 (2021).
334 31 Peters, J. W., Lanzilotta, W. N., Lemon, B. J. & Seefeldt, L. C. X-ray crystal structure
335 of the Fe-only hydrogenase (Cpl) from *Clostridium pasteurianum* to 1.8 angstrom
336 resolution. *Science* **282**, 1853-1858 (1998).
337 32 Maia, L. B., Moura, I. & Moura, J. J. G. Molybdenum and tungsten-containing formate
338 dehydrogenases: Aiming to inspire a catalyst for carbon dioxide utilization. *Inorganica*
339 *Chim. Acta* **455**, 350-363 (2017).
340 33 Dong, G. & Ryde, U. Reaction mechanism of formate dehydrogenase studied by
341 computational methods. *J. Biol. Inorg. Chem.* **23**, 1243-1254 (2018).
342 34 Niks, D. & Hille, R. Molybdenum- and tungsten-containing formate dehydrogenases
343 and formylmethanofuran dehydrogenases: Structure, mechanism, and cofactor
344 insertion. *Protein Sci.* **28**, 111-122 (2019).
345 35 Maia, L. B., Moura, I. & Moura, J. J. G. in *Enzymes for Solving Humankind's Problems:*
346 *Natural and Artificial Systems in Health, Agriculture, Environment and Energy* (eds
347 José J. G. Moura, Isabel Moura, & Luisa B. Maia) 29-81 (Springer International
348 Publishing, 2021).
349 36 Raaijmakers, H. *et al.* Gene Sequence and the 1.8 Å Crystal Structure of the Tungsten-
350 Containing Formate Dehydrogenase from *Desulfolvibrio gigas*. *Structure* **10**, 1261-
351 1272 (2002).

352 37 Page, C. C., Moser, C. C., Chen, X. & Dutton, P. L. Natural engineering principles of
353 electron tunnelling in biological oxidation–reduction. *Nature* **402**, 47-52 (1999).
354 38 Basen, M., Geiger, I., Henke, L. & Müller, V. A Genetic System for the Thermophilic
355 Acetogenic Bacterium *Thermoanaerobacter kivui*. *Appl. Environ. Microbiol.* **84**,
356 e02210-02217 (2018).
357 39 Jain, S., Dietrich, H. M., Müller, V. & Basen, M. Formate is Required for Growth of the
358 Thermophilic Acetogenic Bacterium *Thermoanaerobacter kivui* Lacking Hydrogen-
359 Dependent Carbon Dioxide Reductase (HDCR). *Front. Microbiol.* **11**, 59 (2020).
360 40 Esteve-Núñez, A., Sosnik, J., Visconti, P. & Lovley, D. R. Fluorescent properties of *c*-
361 type cytochromes reveal their potential role as an extracytoplasmic electron sink in
362 *Geobacter sulfurreducens*. *Environ. Microbiol.* **10**, 497-505 (2008).
363 41 Bewley, K. D., Ellis, K. E., Firer-Sherwood, M. A. & Elliott, S. J. Multi-heme proteins:
364 Nature's electronic multi-purpose tool. *Biochim. Biophys. Acta* **1827**, 938-948 (2013).
365 42 Sturm, G. *et al.* A dynamic periplasmic electron transfer network enables respiratory
366 flexibility beyond a thermodynamic regulatory regime. *ISME J.* **9**, 1802-1811 (2015).
367 43 Schaffer, M. *et al.* Optimized cryo-focused ion beam sample preparation aimed at in
368 situ structural studies of membrane proteins. *J. Struct. Biol.* **197**, 73-82 (2017).
369 44 Asano, S., Engel, B. D. & Baumeister, W. In Situ Cryo-Electron Tomography: A Post-
370 Reductionist Approach to Structural Biology. *J. Mol. Biol.* **428**, 332-343 (2016).
371 45 Bäuerlein, F. J. B. & Baumeister, W. Towards Visual Proteomics at High Resolution.
372 *J. Mol. Biol.* **433**, 167187 (2021).
373 46 Schuchmann, K. & Müller, V. Autotrophy at the thermodynamic limit of life: a model
374 for energy conservation in acetogenic bacteria. *Nat. Rev. Microbiol.* **12**, 809-821 (2014).
375 47 Schoelmerich, M. C. & Müller, V. Energy conservation by a hydrogenase-dependent
376 chemiosmotic mechanism in an ancient metabolic pathway. *Proc. Natl. Acad. Sci.*
377 *U.S.A.* **116**, 6329-6334 (2019).

378 48 Schwarz, F. M., Moon, J., Oswald, F. & Müller, V. Biological hydrogen storage and
379 release through multiple cycles of bi-directional hydrogenation of CO_2 to formic acid in
380 a single process unit. *Joule* (in press).
381 49 Debabov, V. G. Acetogens: Biochemistry, Bioenergetics, Genetics, and
382 Biotechnological Potential. *Microbiology* **90**, 273-297 (2021).
383 50 Roger, M., Reed, T. C. P. & Sargent, F. Harnessing *Escherichia coli* for Bio-Based
384 Production of Formate under Pressurized H_2 and CO_2 Gases. *Appl. Environ. Microbiol.*
385 **87**, e00299-00221 (2021).
386
387

388 **Figure 1. Cryo-EM structure of a short HDCR filament.** **a**, Three orthogonal views of the
389 single particle cryo-EM density map, segmented and colored by subunit. **b**, Corresponding
390 views of the atomic model in ribbon representation. [4Fe4S]-clusters are shown as orange and
391 yellow spheres. See also Supplementary Video 1.
392
393
394 **Figure 2. Molecular connectivity in the repeating unit of the HDCR filament.** **a**, Front view
395 of a single HDCR repeating unit in ribbon representation, with protein subunits colored.
396 Cofactor organization between FdhF and the closest HydA2 is diagrammed with edge-to-edge
397 distances in angstroms. Interaction sites of HydA2 with HycB4 and FdhF with HycB3 are
398 enlarged (dashed boxes). **b**, Ribbon models of HycB3 and HycB4, highlighting loop regions
399 that form protein-protein interaction sites. **c**, Purified variants of HDCR (10 µg), each missing
400 different subunits. **d,** *In vitro* catalysis by cytoplasmic fractions containing HDCR_His and
401 HDCR variants (0.3 mg). Top: Hydrogen production from formate (150 mM). Bottom: Formate
402 production from H_2 + CO_2 (80:20 [v:v], 1.1 x 10^5 Pa). HDCR_His was defined as 100 % relative
403 enzyme activity (hydrogen evolution from formate, 75 µmol min^{-1} mg^{-1}; formate production
404 from H_2 + CO_2, 24 µmol min^{-1} mg^{-1}). All data points are mean ± SEM from 3 biologically
405 independent replicates, each with 3 technical replicates. Statistical analysis was performed
406 using one-way analysis of variance (ANOVA) with comparative Tukey post-hoc test
407 (significance level ***p = 0.001).
408
409
410 **Figure 3. Filamentation is mediated by the C-terminal helices of HycB3 and HycB4,**
411 **enabling increased HDCR activity.** **a**, The central spine of HDCR is formed by HycB4 and
412 HycB3. Protein interactions between HycB3 and HycB4 are shown in surface view or pipes
413 and planks representation with enlarged views of the interaction sites between HycB3 and

414 HycB4$_2$ (left), HycB4$_2$ and HycB4$_1$ (middle), as well as HycB4$_1$ and HycB3 (right). The C-
415 terminal helices responsible for filament formation are highlighted. **b,** HDCR_His restores
416 growth of *T. kivui* Δ*hdcr* on glucose. HDCR_HycB4Δ[4Fe4S] IV and HDCR_HycB3ΔC
417 partially rescue Δ*hdcr* but with lower growth rates. WT, wild-type. All data points are mean±
418 SEM; 3 biologically independent experiments. **c**, Separation of purified HDCR variants (300
419 µg) on a Superose 6 Increase 10/300 GL prepacked gel filtration column under anaerobic
420 conditions. V_0, void volume. **d**, Separation of elution fractions (10 µg) from c) in a
421 polyacrylamide gel. 1, HDCR_His; 2, HDCR_HycB4Δ[4Fe4S] IV; 3, HDCR_HycB3ΔC; 4,
422 HDCR_HycB4ΔC. **e**, H_2 evolution from formate (150 mM) and formate production from H_2 +
423 CO_2 in purified HDCR variants (10 µg). HDCR_His was defined as 100 % relative enzyme
424 activity (H_2 evolution from formate, 1273 µmol min^{-1} mg^{-1}; formate production from H_2 + CO_2,
425 826 µmol min^{-1} mg^{-1}). **f,** Separation of purified HDCR_His (300 µg), as described in panel C,
426 and H_2 evolution from formate (150 mM) in four different HDCR_His elution fractions (F1-
427 F4), containing different sizes of filaments (2 µg). All data points are mean ± SEM from 3 (e)
428 or 2 (f) biologically independent replicates, each with 3 technical replicates. Statistical analysis
429 was performed using one-way analysis of variance (ANOVA) with comparative Tukey post-
430 hoc test (significance level ***p = 0.001, **p = 0.01, ns = non-significant).
431
432 **Figure 4. An electron nanowire forms the central spine of the HDCR filament. a**, Front
433 view showing electron connectivity within the repeating unit of the HDCR filament. Subunits
434 are shown in transparent surface representation. The shortest electron transfer pathway between
435 H_2 oxidation and CO_2 reduction is highlighted. **b**, Side views showing electron connectivity
436 within the HDCR filament. The [4Fe4S]-cluster HycB4 IV that is likely relevant for electron
437 transfer between the repeating HDCR units is marked with red boxes. **c**, Model of a
438 dodecameric HDCR filament shown in ribbon representation; subunits are colored as in Fig. 1.

439 **d**, Central electron wire of the modelled HDCR filament, displayed as a transparent surface
440 overlaid with positions of the [4Fe4S]-clusters (orange and yellow spheres).

441

442 **<u>Figure 5</u>. Bundles of HDCR filaments bind to the plasma membrane in native *T. kivui***
443 **cells. a**, **b**, Slices through cryo-tomograms of two wild-type *T. kivui* cells containing HDCR
444 filament bundles (yellow arrowheads: lateral views; orange arrowhead: cross-section view).
445 Slice thickness: 7 nm. HDCR filaments were observed in 22 of 34 WT cellular tomograms. For
446 additional examples, see Extended Data Fig. 8A-F. Inset: cross-section slice of seven bundled
447 filaments from the tomogram and the corresponding slice through the subtomogram average
448 (see panel G for details). **c** and **d**, segmentation models of the tomograms shown in panels A
449 and B, respectively. Purple: bacterial S-layer, gray: plasma membrane, blue: ribosomes, yellow:
450 HDCR filaments. Ribosome and HDCR filament densities were obtained by *in situ*
451 subtomogram averaging and mapped back to their locations in the original tomograms (see
452 Methods for details). **e** and **f**, Side views of the segmentations shown in panels C and D,
453 respectively, depicting the higher-order organization of HDCR filament bundles into complete
454 or partial ring-shaped superstructures attached to the plasma membrane. **g**, the subtomogram
455 average of HDCR filaments (generated from 22 tomograms) shows a bundle of seven filaments.
456 The central filament (orange) is resolved to 17 Å (Extended Data Fig. 9B). **h**, enzymes HydA2
457 and FdhF can be fitted into the average (displayed at lower threshold: 0.3 a.u.), but
458 corresponding densities at the periphery of the filament are not as well resolved. **i**, the core of
459 the central filament in the average is well resolved (displayed at threshold: 0.7 a.u.) and fits the
460 [4Fe4S] electron nanowire formed by proteins $HycB4_1$, $HycB4_2$ and HycB3. See also
461 Supplementary Video 2.

462

463 **Methods**

464 *T. kivui* cultivation, preparation of cytoplasmic fractions, and purification of the HDCR
465 complex.

466 *Thermoanaerobacter kivui* LKT-1 (DSM 2030, acquired by the DSMZ - German Collection of
467 Microorganisms and Cell Cultures GmbH, Germany) and all its derivatives were cultivated
468 heterotrophically at 66 °C in complex medium with 28 mM glucose or 28 mM glucose and 50
469 mM formate as carbon source as described previously[39]. Strain authentication was routinely
470 performed via PCR. For that, 1 ml of fresh culture was centrifuged and washed twice with
471 buffer A (25 mM Tris/HCl, 20 mM $MgSO_4$, 20 % glycerol [v/v], 0.5 mM dithioerythritol, 4 µM
472 resazurin, pH 7.5), following resuspension in 50 µl buffer A. 1 µl was used as a template for
473 PCR, using 25 µl reactions containing Q5 High-Fidelity DNA Polymerase (New England
474 Biolabs, Ipswich, MA, USA) according to manufacturer specifications, using primers Pseq5-
475 Pseq11 (forward primers) and Pseq12-Pseq13 (reverse primers) targeting specific *hdcr* genes.
476 For primer sequences, please refer to Supplementary table 5. PCR products were analyzed via
477 gel electrophoresis and verified against control PCR reactions using purified *hdcr* DNA
478 sequence as template. For growth studies, cultures were cultivated in 120 ml serum bottles
479 containing 50 ml complex media supplemented with 28 mM glucose. Growth was monitored
480 by determining the optical density at 600 nm with a UV/Vis spectrophotometer. Purification of
481 native HDCR from wild-type *T. kivui* was performed as previously reported[3]. Cells containing
482 HDCR variants were harvested in late exponential phase and cytoplasmic fractions were
483 generated as described by Schwarz *et al.*[3], except disrupted cells were directly ultra-centrifuged
484 at 184,000×*g* for 45 min at 10 °C to eliminate cell debris and membranes from the cytoplasmic
485 fraction. The supernatant was used for purification of the His_6-tagged HDCR with a metal
486 affinity column (Ni-NTA, Qiagen, Hilden). Purification was performed under strictly anoxic
487 conditions. The Ni-NTA material was equilibrated with buffer B (25 mM Tris/HCl, 20 mM
488 $MgSO_4$, 20 % glycerol [v/v], 0.5 mM dithioerythritol, 4 µM resazurin, 30 – 50 mM imidazole,

489 pH 7.5) and incubated with the cytoplasmic fraction for 45 min at 4 °C before elution with
490 buffer C (same as buffer B, but 150 mM imidazole) was performed.
491
492 Cryo-electron microscopy sample preparation and imaging.
493 For cryo-EM sample preparation, natively purified HDCR was used at a concentration of 1
494 mg/ml. The sample preparation chamber of a Vitrobot was flooded with nitrogen gas to replace
495 an oxygenic atmosphere, and 4.5 µl of the protein were applied to glow discharged Quantifoil
496 2.1/1 grids using a Hamilton-syringe. The sample was incubated for 20 s in a Vitrobot Mark IV
497 (Thermo Fisher) at 100 % humidity and 4 °C, then blotted for 3.5 s with force 4 and plunge
498 frozen in liquid ethane, cooled by liquid nitrogen. Cryo-EM data was acquired with an FEI
499 Titan Krios transmission electron microscope using SerialEM (version 3.8) software[51]. Movie
500 frames were recorded at a nominal magnification of 105,000X (calibrated object pixel size of
501 1.09 Å) using a post-GIF K3 direct electron detector (Gatan). The total electron dose of ~52
502 electrons per $Å^2$ was fractionated over 40 frames. Cryo-EM micrographs were processed on the
503 fly using the Focus software package[52] and only kept if they passed the selection criteria (iciness
504 < 1.05, drift 0.4 Å < x < 70 Å, defocus 0.5 µm < x < 5.5 µm, estimated CTF resolution < 5 and
505 over Å). Micrograph frames were aligned using MotionCor2 (version 1.4.0)[53] and the contrast
506 transfer function (CTF) for aligned frames was determined using GCTF and CTFFIND
507 4.1.14[54,55].
508
509 Image processing, classification and refinement.
510 A total of 33,853 micrographs passed the selection criteria and were further processed in
511 CryoSPARC[56]. A subset of 1000 micrographs were used in an iterative reference-free 2D
512 classification procedure to optimize parameters in the template picker (Extended Data Fig. 1).
513 After applying the optimized parameters on the entire dataset, two subsequent rounds of
514 reference-free 2D classification were carried out to remove obvious non-particle candidates,

515 yielding a total of 3,134,127 particles. Particles were extracted using a box size of 352 pixels.
516 Using a subset of 50,000 particles, an *ab-initio* initial model was calculated and used for two
517 consecutive rounds of 3D classification. Mainly short filaments varying in length between one
518 and three repeating units were present in the dataset. However, only classes containing the
519 longest filaments were selected for further refinement, as the other classes exhibited strong
520 preferred orientation bias. The class consisting of HDCR filaments with three repeating units
521 contained 719,937 particles, which were refined using the non-uniform refinement algorithm[57]
522 to yield a resolution of 3.44 Å. Further optimization of per-particle CTF and global CTF
523 parameters resulted in a final model with an estimated resolution of 3.4 Å and a sharpening B-
524 factor of -123.1 $Å^2$. Despite the marginal increase in numerical resolution, the map quality was
525 significantly improved and thus used for modeling of the HDCR filaments. Additional
526 refinement approaches including density subtraction, local refinement and per-frame
527 reconstructions to compensate for electron damage did not lead to noteworthy improvements
528 despite multiple attempts. Directional FSC curves and map anisotropy were assessed using the
529 3DFSC server[58].
530
531 <u>Model building and refinement.</u>
532 Structural models for the [4Fe4S] proteins HycB3 and HycB4 that form the core of the filament
533 were built *de novo* using Coot[59] and refined against the cryo-EM map using the
534 phenix.real_space_refine routine in the PHENIX software package[60]. Structural models for
535 HydA2 and FdhF were predicted with AlphaFold[30]. The models were fitted in the electron
536 density map as rigid-bodies with UCSF Chimera[61] and were subsequently manually adjusted
537 and rebuilt using Coot[59] and PHENIX. FdhF in particular has larger areas with increased
538 flexibility and lower local resolution that prevented *de novo* modeling of the non-protein W-
539 bisPGD cofactor. Due to a very high structural similarity and conservation of the active site
540 architecture with the tungsten-containing formate dehydrogenase from *Desulfovibrio gigas*

541 (PDB: 1H0H), its cofactor coordinates were extracted and used for visualization purposes
542 (Extended Data Fig. 5). The [4Fe4S]-clusters and H-clusters were refined using PHENIX. For
543 refining the H-clusters in the complex, a geometry file containing the coordinates of the H-
544 cluster (RCSB ligand ID - 402) was used to generate a restraint CIF file using the electronic
545 Ligand Builder and Optimization Workbench (eLBOW) tool[62] integrated in the PHENIX work
546 suite. This CIF file was then used as an input to constrain the real space refinement. The
547 statistical quality of the final protein model was assessed using MOLPROBITY[63]. Figures were
548 prepared using PyMOL 2.3[64] or UCSF ChimeraX 1.3[65].
549
550 <u>Negative staining electron microscopy.</u>
551 For negative staining, glow discharged grids (Quantifoil holey carbon grids R 2/1, Cu 200 mesh,
552 2 nm carbon support) were prepared in an anaerobic tent with a gas composition of 95 % N_2
553 and 5 % H_2 and stained with 2 % uranyl acetate. Images of the HDCR filaments were acquired
554 on a FEI Titan Halo operated at 300 kV equipped with a Falcon 3EC direct electron detector
555 using the EPU software package at a nominal magnification of 45,000X (2.37 Å/pixel).
556
557 <u>Design and overproduction of HDCR derivatives.</u>
558 Overproduction of the HDCR variants was performed using pMU131 as a basic plasmid[66],
559 extended with the genetic constructs for HDCR variants based on the genomic sequence of the
560 HDCR operon from *T. kivui*. Expression of all HDCR derivatives were under control of the
561 promoter of the S-layer protein from *T. kivui*[39]. For metal affinity purification, a 6×Histidine-
562 tag (His_6) was added C-terminally at the *hydA*2 sequence or N-terminally at the *fdhF* sequence
563 if the *hydA2* sequence was missing in the construct. As an initial plasmid and basis for
564 construction of HDCR derivatives, pHD001 was generated, carrying the genetic information of
565 the complete HDCR operon including the terminator sequence. The pMU131 backbone was
566 amplified using primers P11 and P12. All primers used in this study are displayed in

567 Supplementary Table 5. For amplification of the S-layer promoter sequence, primers P1 and P2
568 were used with pPB5[67] as template DNA. The first part of the *hdcr* gene sequence, including
569 the His_6 tag, was amplified using primers P3 and P4 with genomic DNA of *T. kivui* as the DNA
570 template. The remaining HDCR operon, including the terminator sequence, was amplified
571 using primers P5 and P6, again with pPB5 as the DNA template. The three DNA insert
572 fragments were cloned into the amplified pMU131 backbone using Gibson assembly[68]. Plasmid
573 pHD001 was used as a template to generate HDCR variants pHD020 (primer pair P47 and P48),
574 pHD026 (P55 and P56), pHD028 (P57 and P58), pLR002 (PLR3 and PLR4), pLR003b (PLR7
575 and PLR8), pLR004 (PLR15 and PLR16), pRT8 (PRT7 and PRT8) and pRT9 (PRT9 and
576 PRT10). For pLR002c, primers PLR11b and PLR12b were used with pLR002 as template
577 DNA. Based on pLR002c, plasmid pHD015 was amplified (P39 and P40). Plasmid pHD024
578 was generated using pLR003b and primers PLR11b and PLR12b. Cyclization of the amplified
579 DNA fragments was performed using NEBuilder® HiFi DNA Assembly Master Mix (pHD001,
580 pHD015, pHD020, pHD024, pLR002, pLR002c, pLR003b, pLR004) or KLD Enzyme Mix
581 (pHD026, pHD028, pRT8, pRT9) (both North England Biolabs, Ipswich (MA), USA).
582 The resulting plasmids (Supplementary Table 4) were transformed into *Escherichia coli* 10-
583 beta (New England Biolabs, NEB) or DH5α (NEB) for generating high copy numbers of the
584 plasmid, followed by plasmid isolation and transformation into *T. kivui* Δ*hdcr* as described by
585 Basen *et al*.[38] (Supplementary Table 3).
586
587 <u>Analytical methods.</u>
588 Protein concentration was determined by Bradford assay[69]. Protein separation was performed
589 in 16.5 % polyacrylamide gels, and proteins were stained with Coomassie brilliant blue G250.
590 Source data of polyacrylamide gels are provided in the Supplementary Information file.
591 Following separation of purified HDCR_His subunits, proteins were identified via Matrix-
592 Assisted Laser Desorption/Ionization - Time of Flight Mass Spectrometry (MALDI-TOF;

593 ETH Zürich). Size exclusion chromatography was performed as described by Schwarz *et al.*[3]
594 and analyzed with UNICORN 5.31 software.
595
596 Measurement of enzyme activity.
597 Methylviologen-dependent formate dehydrogenase and hydrogenase activity, as well as
598 hydrogen production from formate, and formate production from $H_2 + CO_2$, were measured as
599 described before[2,3]. The one exception is that, unless otherwise stated, the reaction temperature
600 was set to 64 °C, since this is the physiological growing temperature of *T. kivui*. In all enzyme
601 assays, the reaction buffer was pre-incubated at the target temperature. 0.3 mg of cell-free
602 extract (cytoplasmic fraction) or 0.01 mg of purified HDCR proteins were used for activity
603 measurements, if not stated otherwise. pH and temperature optima analysis as well as
604 cytoplasmic H_2-production from formate in different HDCR variants (Extended Data Fig. 7G)
605 was performed in biological triplicates, each in technical duplicate (total N = 6). Formate
606 production from $H_2 + CO_2$ in cytoplasmic fractions of different HDCR variants (Extended Data
607 Fig. 7H) was performed in technical triplicates (N = 3). H_2-production from formate in different
608 filament sizes of HDCR_His was performed in biological duplicate, each in technical triplicates
609 (N = 6). All other enzymatic measurements were performed in biological triplicates, each with
610 technical triplicates (total N = 9). Photometric data was analyzed with WinASPECT 2.5.0.0
611 software, gas chromatography data was analyzed using TC Navigator 6.3.2 software.
612
613 Cryo-electron tomography sample preparation, FIB-milling and acquisition.
614 Cultures (OD_{600} = 0.1) of *T. kivui* wild-type strain and HDCR knockout strain (Δ*hdcr*) were
615 grown for 6 h at 66 °C until early exponential growth stage (OD_{600} = ~0.25). Cultures were then
616 centrifuged briefly to concentrate the cells to OD_{600} = ~5 and used immediately for plunge
617 freezing. To avoid a detrimental contact between the anaerobic bacteria and oxygen, cell
618 handling and loading of the micro-pipette was performed in a nitrogen atmosphere. To achieve

619 this, a cardboard box with a small cutout for handling was constructed and sealed with tape. A
620 raft of styrofoam was placed at the bottom of the box, and all the necessary equipment was put
621 on top of the raft. Concentrated bacteria cultures were kept on a preheated metal block to
622 maintain proper temperature of the culture during the plunging procedure. The box was filled
623 with liquid nitrogen. Continuous evaporation of the nitrogen, and the volume expansion
624 resulting from the liquid-to-gas transition, ensured the exclusion of air (and therefore the
625 oxygen). The anaerobicity of the environment was controlled with a candle flame at regular
626 intervals. The pipette tip was purged in the nitrogen atmosphere before every use. 4 µl of *T.*
627 *kivui* wild-type or Δ*hdcr* culture was directly placed on the EM grid and blotted for 10 seconds
628 with a blot force of 10 onto R 2/1 carbon-foil 200-mesh copper EM grids (Quantifoil Micro
629 Tools) and plunge frozen in a liquid ethane/propane mixture using a Vitrobot Mark 4 (Thermo
630 Fisher Scientific). Afterwards, grids were clipped into Autogrid support rings with a cut-out
631 that allows access to the ion beam at low angle (Thermo Fisher Scientific) and stored in liquid
632 nitrogen until used for FIB milling. Cryo-FIB milling was performed as described previously[43]
633 with an Aquilos dual-beam FIB/SEM instrument (Thermo Fisher Scientific). In the FIB/SEM
634 chamber, grids were coated with a layer of organometallic platinum using a gas injection system
635 to protect the sample surface. Micro-expansion joints (relief cuts) were milled to prevent
636 lamella from bending[70] A gallium ion beam was used for the milling. Due to the small size of
637 individual bacteria, carpets consisting of ~2-3 layers of cells were milled at low angle (14-15°)
638 to form short lamellae of 150-200 nm thickness. After milling, grids were transferred into a
639 Titan Krios 300 kV microscope (Thermo Fisher Scientific), operating with a post-column
640 energy filter (Quantum, Gatan), and a direct detector camera (K2 summit, Gatan). Tilt-series
641 were acquired using SerialEM 3.8 software[51] and a dose-symmetric tilt scheme[71], with 2° steps
642 totaling 60 tilts per series. Each image was recorded in counting mode with 8 frames per second
643 and an object pixel size of at 3.52 Å. The target defocus of individual tilt-series ranged from -

644 3.5 to -5 µm. The total accumulated dose deposited on each tilt-series ranged from 90 to 120 e^-
645 /Å^2.
646

647 Tomogram preprocessing and reconstruction.

648 All tilt-series were preprocessed using the TOMOMAN pipeline (v0.6)
649 [https://github.com/williamnwan/TOMOMAN/][72] and custom MATLAB scripts. Raw frames
650 were aligned using MotionCor2 (version 1.4.0)[53]. Tilt-series were dose-weighted[73] and cleaned
651 to remove bad tilts. The assembled tilt-series were aligned with patch tracking[74], and
652 tomographic volumes (binned 4 times; 14.08 Å pixel size) were reconstructed by weighted back
653 projection in IMOD (version 4.11.1)[75]. To remove noise and enhance the contrast, the Cryo-
654 CARE denoising filter[76] was applied to the bin4 tomograms. The IMOD 3dmod viewer was
655 used to capture images of tomographic slices. Tomogram segmentation was performed in
656 Amira software (Thermo Fisher Scientific), using a combination of automated membrane
657 detection from the TomoSegMemTV software package[77] and manual segmentation.
658

659 Subtomogram averaging.

660 HDCR filaments were identified in selected denoised tomograms and manually traced using
661 the 3dmod viewer in IMOD (version 4.11.1). The subtomogram averaging package STOPGAP
662 0.7.1 [https://github.com/williamnwan/STOPGAP/][78] was used to oversample the picked
663 positions along the filaments using fitted splines and extract subvolumes from tomograms
664 which were 3D CTF corrected using NovaCTF[79]. Alignment and averaging of these
665 subtomograms yielded a native reference that contained a bundle of HDCR filaments. The
666 central filament of this bundle was masked out and subsequently used for template matching
667 (TM) in STOPGAP using an angular search with a 15° step and a resolution limit of 75 Å. TM
668 score maps were segmented and cleaned in UCSF Chimera[61] using the Segger plugin[80] to focus
669 only on areas containing HDCR filament bundles. Volumes were then extracted with

670 STOPGAP's MATLAB scripts using a TM score map peak-to-peak distance of 4 pixels at bin4
671 (5.6 nm), which is slightly shorter than the measured repeat length of HDCR filaments *in situ*
672 (7 nm), to avoid accidental exclusion of true positives. A box size of 48 pixels at bin4 was
673 chosen in order to enclose roughly nine HDCR subunits along the central filament, plus six
674 neighboring filaments in the bundle. This approach yielded 12,524 subvolumes from 22
675 tomograms. Subtomogram averaging and alignment was further carried out in STOPGAP until
676 convergence, with intermediate score-based exclusion of false or badly aligning particles. An
677 overview of the data processing pipeline employed is shown in Extended Data Fig. 9A. The
678 maximum resolution used for particle alignment was 34 Å in order to prevent overfitting. The
679 final reconstruction at bin2 (box size: 96 pixels) contained 6,727 particles and was resolved to
680 17 Å according to Fourier shell correlation (FSC)[81] at the 0.143 threshold criterion[82] using a
681 soft mask focusing on the central filament (Extended Data Fig. 9B). To minimize inflation of
682 the FSC due to the shared signal from overlapping neighboring particles, the dataset was split
683 into two half-sets based on 100 consecutive chunks of particles[83]. The average was then mapped
684 back into the original position of the particles in the tomograms using the "Place Object" script[84]
685 in UCSF Chimera. Renderings of mapped back particles and segmentations were created in
686 UCSF ChimeraX[65]. Fitting of the atomic model obtained by single-particle cryo-EM was done
687 in UCSF Chimera. Helical symmetry parameters were measured based on the fitted model
688 (Extended Data Fig. 9C).
689

690 **Additional references**

691 51 Mastronarde, D. N. Automated electron microscope tomography using robust prediction
692 of specimen movements. *J. Struct. Biol.* **152**, 36-51 (2005).
693 52 Biyani, N. *et al.* Focus: The interface between data collection and data processing in
694 cryo-EM. *J. Struct. Biol.* **198**, 124-133 (2017).

695 53 Zheng, S. Q. *et al.* MotionCor2: anisotropic correction of beam-induced motion for
696 improved cryo-electron microscopy. *Nat. Methods* **14**, 331-332 (2017).
697 54 Rohou, A. & Grigorieff, N. CTFFIND4: Fast and accurate defocus estimation from
698 electron micrographs. *J. Struct. Biol.* **192**, 216-221 (2015).
699 55 Zhang, K. Gctf: Real-time CTF determination and correction. *J. Struct. Biol.* **193**, 1-12
700 (2016).
701 56 Punjani, A., Rubinstein, J. L., Fleet, D. J. & Brubaker, M. A. cryoSPARC: algorithms
702 for rapid unsupervised cryo-EM structure determination. *Nat. Methods* **14**, 290-296
703 (2017).
704 57 Punjani, A., Zhang, H. & Fleet, D. J. Non-uniform refinement: adaptive regularization
705 improves single-particle cryo-EM reconstruction. *Nat. Methods* **17**, 1214-1221 (2020).
706 58 Tan, Y. Z. *et al.* Addressing Preferred Specimen Orientation in Single-Particle Cryo-
707 EM through Tilting. *Nat. Methods* **14**, 793-796 (2017).
708 59 Emsley, P. & Cowtan, K. Coot: model-building tools for molecular graphics. *Acta*
709 *Crystallogr. D. Biol. Crystallogr.* **60**, 2126-2132 (2004).
710 60 Afonine, P. V. *et al.* Real-space refinement in *PHENIX* for cryo-EM and
711 crystallography. *Acta Crystallogr. D. Biol. Crystallogr.* **74**, 531-544 (2018).
712 61 Pettersen, E. F. *et al.* UCSF Chimera--a visualization system for exploratory research
713 and analysis. *J. Comput. Chem.* **25**, 1605-1612 (2004).
714 62 Moriarty, N. W., Grosse-Kunstleve, R. W. & Adams, P. D. electronic Ligand Builder
715 and Optimization Workbench (eLBOW): a tool for ligand coordinate and restraint
716 generation. *Acta Crystallogr. D. Biol. Crystallogr.* **65**, 1074-1080 (2009).
717 63 Chen, V. B. *et al.* *MolProbity*: all-atom structure validation for macromolecular
718 crystallography. *Acta Crystallogr. D. Biol. Crystallogr.* **66**, 12-21 (2010).
719 64 Delano, W. L. (2002). *The PyMOL molecular graphics system*, Schrödinger.

720 65 Goddard, T. D. *et al.* UCSF ChimeraX: Meeting modern challenges in visualization and
721 analysis. *Protein Sci.* **27**, 14-25 (2018).
722 66 Shaw, A. J., Hogsett, D. A. & Lynd, L. R. Natural Competence in *Thermoanaerobacter*
723 and *Thermoanaerobacterium* Species. *Appl. Environ. Microbiol.* **76**, 4713-4719 (2010).
724 67 Benner, P. *Proteinproduktion im thermophilen, acetogenen Bakterium*
725 *Thermoanaerobacter kivui.* Bachelor thesis, Goethe University Frankfurt am Main,
726 (2016).
727 68 Gibson, D. G. *et al.* Enzymatic assembly of DNA molecules up to several hundred
728 kilobases. *Nat. Methods* **6**, 343-345 (2009).
729 69 Bradford, M. M. A rapid and sensitive method for the quantification of microgram
730 quantities of protein utilizing the principle of proteine-dye binding. *Anal. Biochem.* **72**,
731 248-254 (1976).
732 70 Wolff, G. *et al.* Mind the gap: Micro-expansion joints drastically decrease the bending
733 of FIB-milled cryo-lamellae. *J. Struct. Biol.* **208**, 107389 (2019).
734 71 Hagen, W. J. H., Wan, W. & Briggs, J. A. G. Implementation of a cryo-electron
735 tomography tilt-scheme optimized for high resolution subtomogram averaging. *J.*
736 *Struct. Biol.* **197**, 191-198 (2017).
737 72 Wan, W. (2020). *williamnwan/TOMOMAN: TOMOMAN 08042020 (Version*
738 *08042020)*, Zenodo. https://doi.org/10.5281/zenodo.4110737.
739 73 Grant, T. & Grigorieff, N. Measuring the optimal exposure for single particle cryo-EM
740 using a 2.6 Å reconstruction of rotavirus VP6. *Elife* **4**, e06980 (2015).
741 74 Mastronarde, D. N. & Held, S. R. Automated tilt series alignment and tomographic
742 reconstruction in IMOD. *J. Struct. Biol.* **197**, 102-113 (2017).
743 75 Kremer, J. R., Mastronarde, D. N. & McIntosh, J. R. Computer visualization of three-
744 dimensional image data using IMOD. *J. Struct. Biol.* **116**, 71-76 (1996).

745 76 Buchholz, T., Jordan, M., Pigino, G. & Jug, F. Cryo-CARE: Content-Aware Image
746 Restoration for Cryo-Transmission Electron Microscopy Data. *2019 IEEE 16th*
747 *International Symposium on Biomedical Imaging (ISBI 2019)*, 502-506 (2019).
748 77 Martinez-Sanchez, A., Garcia, I., Asano, S., Lucic, V. & Fernandez, J. J. Robust
749 membrane detection based on tensor voting for electron tomography. *J. Struct. Biol.*
750 **186**, 49-61 (2014).
751 78 Wan, W. (2020). *williamnwan/STOPGAP: STOPGAP 0.7.1 (0.7.1)*, Zenodo.
752 https://doi.org/10.5281/zenodo.3973664.
753 79 Turoňová, B., Schur, F. K. M., Wan, W. & Briggs, J. A. G. Efficient 3D-CTF correction
754 for cryo-electron tomography using NovaCTF improves subtomogram averaging
755 resolution to 3.4Å. *J. Struct. Biol.* **199**, 187-195 (2017).
756 80 Pintilie, G. D., Zhang, J., Goddard, T. D., Chiu, W. & Gossard, D. C. Quantitative
757 analysis of cryo-EM density map segmentation by watershed and scale-space filtering,
758 and fitting of structures by alignment to regions. *J. Struct. Biol.* **170**, 427-438 (2010).
759 81 Harauz, G. & van Heel, M. Exact filters for general geometry three dimensional
760 reconstruction. *Optik* **73**, 146-156 (1986).
761 82 Rosenthal, P. B. & Henderson, R. Optimal Determination of Particle Orientation,
762 Absolute Hand, and Contrast Loss in Single-particle Electron Cryomicroscopy. *J. Mol.*
763 *Biol.* **333**, 721-745 (2003).
764 83 Grant, T., Rohou, A. & Grigorieff, N. *cis*TEM, user-friendly software for single-particle
765 image processing. *Elife* **7**, e35383 (2018).
766 84 Qu, K. *et al.* Structure and architecture of immature and mature murine leukemia virus
767 capsids. *Proc. Natl. Acad. Sci. U. S. A.* **115**, E11751-E11760 (2018).
768

Data availability

Cryo-EM maps, as well as cryo-ET subtomogram averages and cellular tomograms are available in the Electron Microscopy Data Bank with the accession codes EMD – 14169 (Cryo-EM maps), EMD – 15053 (subtomogram average of HDCR), EMD – 15054 (sub tomogram average of *T. kivui* ribosomes), EMD – 15055 (Fig. 5b tomogram), EMD – 15056 (Fig. 5a tomogram). Raw electron tomography data are available on the Electron Microscopy Public Image Archive (EMPIAR – 11058). Atomic models of HDCR are available in the Protein Data Bank (PDB – 7QV7). Structural and sequence data used for comparison with HDCR subunits are available in the Protein Data Bank (PDB – 3C8Y, iron hydrogenase from *Clostridium pasteurianum*; PDB – 1H0H, W-containing formate dehydrogenase from *Desulfovibrio gigas*).

Funding:

J.M.S. acknowledges the DFG for early career support by an Emmy Noether grant (SCHU 3364/1-1). Work from the V.M. laboratory was supported by the European Research Council (Acetogens, grant agreement no. 741791). Work from the B.D.E. laboratory was supported by a DFG grant (EN 1194/1–1, part of FOR 2092), Helmholtz Munich and the University of Basel. H.M.D. was funded by a fellowship from Deutsche Bundesstiftung Umwelt (DBU) (Ph.D. grant no. 20016/446). R.D.R. acknowledges funding from the Alexander von Humboldt Foundation and a non-stipendiary fellowship from EMBO.

Acknowledgements:

We thank Daniel Bollschweiler and Tillman Schäfer at the MPIB cryo-EM facility for single particle cryo-EM data acquisition, Jan Zarzycki for help with model building, Manon Demulder for help with FIB milling, and Hugo van den Hoek, Florian Beck, Philipp Erdmann, Sagar Khavnekar and William Wan for scripts and advice with cryo-ET analysis. We are grateful to

794 Elena Conti, Jürgen Plitzko and Wolfgang Baumeister for access to state-of-the-art FIB and
795 TEM instrumentation, to Philipp Benner and Mirko Basen for their gift of pPB5 and stimulating
796 discussions, and to Luna Ribaric for help in preparing pLR2, pLR2c, pLR3b and pLR4.
797 Calculations were performed at the Max Planck Institute for Biochemistry computing cluster in
798 Martinsried, Germany, and at the sciCORE (http://scicore.unibas.ch/) scientific computing
799 center at the University of Basel.

800

801 **Author contributions**

802 H.M.D., B.D.E, J.M.S. and V.M. designed and coordinated the experiments; H.M.D, R.T. and
803 F.M.S. expressed and purified the proteins; H.M.D and R.T. carried out enzymatic assays.
804 S.K.S. and J.M.S. collected and processed cryo-EM data; A.K., S.K.S. and J.M.S. built and
805 refined models; H.M.D., R.D.R., A.K., J.M.S. and V.M. analyzed and interpreted the functional
806 and structural data; W.W. and J.W. performed FIB milling and cryo-ET data acquisition; R.D.R.
807 and J.W. processed and analyzed the cryo-ET data; A.K. and J.W. performed the negative stain
808 imaging; J.M.S., B.D.E, and V.M. wrote the manuscript together with all other authors.

809

810 **Declaration of Interests**

811 The authors declare no competing interests.

812

813 **Supplementary information** is available for this paper.

814 Correspondence and requests for materials should be addressed to ben.engel@unibas.ch,
815 vmueller@bio.uni-frankfurt.de, or jan.schuller@synmikro.uni-marburg.de.

816

817 **Extended Data Figure legends**

818 **Extended Data Fig. 1. Cryogenic electron microscopy (Cryo-EM) data collection and**
819 **analysis. a**, A representative cryo-EM micrograph (N = 33,853) collected on a FEI Titan Krios

820 microscope (scale bar: 50 nm), operated at 300 kV and equipped with a K3 camera. **b**,
821 Reference-free 2D class averages revealing the short HDCR filament in multiple orientations.
822 **c**, Overview of the cryo-EM data processing scheme. **d**, Angular distribution of the particles
823 used for the final round of refinement. **e**, Plot showing the global resolution and sphericity of
824 the final HDCR reconstruction, calculated using the "Remote 3DFSC Processing Server" web
825 interface[58]. A sphericity of 0.939 indicates an isotropic particle orientation. **f**, Local resolution
826 as calculated by CryoSPARC mapped on the refined density (left: bottom and side view, right:
827 cut-open view of central section).

828

829 **Extended Data Fig. 2. Filament bundling of purified HDCR used for cryo-EM and**
830 **negative staining. a-d**, Longer HDCR filaments were occasionally observed in cryo-EM
831 micrographs of the purified HDCR preparation. These filaments generally grouped together as
832 bundles with varying filament length, impeding structural analysis. Representative images from
833 33,853 micrographs collected. Micrograph recording was performed as described in Extended
834 Data Fig. 1. Scale bar: 50 nm. **e-f**, Representative negative stain images of HDCR_His from F2
835 of Fig. 3F (N = 8), showing large filament bundles. Scale bars: 100 nm.

836

837 **Extended Data Fig. 3. Model Quality. a**, Structural models of the enzymatic active subunits
838 in their electron density. FdhF domain IV is flexible (see Extended Data Figure 5). The same
839 colors are used as in Fig. 1. **b**, Representative regions of the HDCR complex and surrounding
840 electron density maps are shown. Subunits and residue numbers are specified. Snapshots are
841 shown for the density of both folded and cofactor binding regions.

842

843 **Extended Data Fig. 4. Structural conservation of HydA2. a**, Structural model of HydA2. **b**,
844 Superposition of HydA2 (blue) with the closest homolog [FeFe]-hydrogenase from *Clostridium*
845 *pasteurianum* and zoom-in of the active site. **c**, Fit of the H-Cluster (PDB: 3C8Y) in the electron
846 density. **d**, Sequence alignment of HydA2 with the [FeFe]-hydrogenase CpI from *Clostridium*
847 *pasteurianum*. Conserved residues are highlighted with color, with darker shades of blue
848 indicating high conservation. This alignment shows high conservation of the cap domain.
849 Functional and cofactor-coordinating residues are marked according to the legend on the right
850 side, revealing a full conservation of H-Cluster coordination.

851

852 **Extended Data Fig. 5. Structural conservation of FdhF. a**, Structural model of domains I-
853 III of FdhF as built from the cryo-EM density. Close up of the [4Fe4S]-cluster fitted into its
854 map (mesh), demonstrating map quality. **b**, Superposition of FdhF (green) with the tungsten-
855 containing formate dehydrogenase from *Desulfovibrio gigas* (pink, PDB: 1H0H). Close up of
856 the tungsten and pterin guanine dinucleotide binding site reveals high structural conservation.
857 Fit of the W-bisPGD cofactors (1H0H) in the electron density. **c**, Composite model of FdhF:
858 domains I-III were built from the cryo-EM density (as in panel A), and domain IV as well as
859 the W-bisPGD cofactors were derived from homology. **d**, Sequence alignment of FdhF with
860 the tungsten-containing formate dehydrogenase from *Desulfovibrio gigas*. Conserved residues
861 are highlighted, with darker shades of blue indicating high conservation. This alignment shows
862 that all domains are highly conserved. Functional and cofactor-coordinating residues are
863 marked according to the legend on the right side, revealing conservation of W-bisPGD cofactor
864 coordination. For more details on conserved W-bisPGD coordinating amino acids, see also
865 Supplementary Table 2.

866

867 **Extended Data Fig. 6. HDCR_His complements the native HDCR enzyme activity. a,**
868 Purified HDCR (10 µg) from wild-type *T. kivui* (HDCR native) and from the overproduction
869 strain HDCR_His have identical protein subunits. **b,** Isolated native HDCR and the HDCR_His
870 tested for H_2 evolution from formate and formate production from $H_2 + CO_2$. Data for "HDCR
871 native" are reproduced from Schwarz *et al.*[3]. Hydrogen production from formate (150 mM)
872 catalyzed by 10 µg isolated HDCR_His. Formate production as described before, but $H_2 + CO_2$
873 (80:20 [v:v], 1.1 x 10^5 Pa) was used as a substrate. **c**, Hydrogen production from formate (150
874 mM) catalyzed by 0.3 mg of cytoplasmic fractions of WT (HDCR native) and HDCR_His *T.*
875 *kivui* strains. All data points are mean ± SEM, taken from 3 biologically independent replicates,
876 each with 3 technical replicates. Statistical analysis was performed using one-way analysis of
877 variance (ANOVA) with comparative Tukey post-hoc test (significance level ***p = 0.001).
878
879 **Extended Data Fig. 7. Catalytic properties of HDCR variants. a-d,** Characterization of the
880 pH- and temperature-dependence of HDCR native (squares) and HDCR_His (circles). **a** and **c**,
881 Methylviologen-dependent hydrogenase activity with H_2 or **b** and **d,** formate dehydrogenase
882 activity with formate as electron donor. Data for HDCR native are reproduced from Schwarz *et*
883 *al.*[3]. 0.03 µg (H_2:MV-oxidoreductase activity) or 3 µg (formate:MV-oxidoreductase activity)
884 of HDCR_His were incubated in reaction buffer at 64 °C. 10 mM methylviologen was used as
885 an electron acceptor, and reduction of methylviologen was monitored at 604 nm. MV,
886 methylviologen. **e-f,** Functionality of catalytical subunits in HDCR variants. **e**, Methylviologen-
887 dependent hydrogenase activity with H_2 or **f**, formate dehydrogenase activity with formate as
888 an electron donor. 3 µg (H_2:MV-oxidoreductase activity) or 30 µg (formate:MV-
889 oxidoreductase activity) of cytoplasmic fractions containing HDCR variants were incubated in
890 reaction buffer at 64 °C. 10 mM methylviologen was used as an electron acceptor, and reduction
891 of methylviologen was monitored at 604 nm. 100 % corresponds to the activity of the complete
892 HDCR_His complex (H_2:MV-oxidoreductase activity 301 µmol min^{-1} mg^{-1}; formate:MV-

893 oxidoreductase activity 40 µmol min^{-1} mg^{-1}). MV, methylviologen. **g)** Hydrogen production
894 from formate of selected HDCR variants. **h)** Formate production from H_2 + CO_2 of selected
895 HDCR variants. HDCR_His was defined as 100 % relative enzyme activity (hydrogen
896 evolution from formate, 83 µmol min^{-1} mg^{-1}; formate production from H_2 + CO_2, 25 µmol min^{-1}
897 mg^{-1}). All data points are mean ± SEM, taken from 3 (a-g) or 1 (h) biologically independent
898 replicates, each with 3 (e,f,h) or 2 (a,b,c,d,g) technical replicates. Statistical analysis was
899 performed using one-way analysis of variance (ANOVA) with comparative Tukey post-hoc test
900 (significance level ***p = 0.001). For further methods details, see Supplementary Information.
901
902 **Extended Data Fig. 8. Cryo-ET of wild-type and Δ*hdcr* mutant *T. kivui* cells confirms**
903 **identity of HDCR. a-f**, Slices through cryo-tomograms of wild-type (WT) *T. kivui* cells
904 containing HDCR filament bundles (yellow arrowheads). HDCR filaments were observed in
905 22 of N = 34 WT tomograms. **g-l**, Slices through cryo-tomograms of mutant *T. kivui* cells in
906 which the genes coding for HDCR proteins were deleted (Δ*hdcr*). No filaments were observed
907 in N = 34 Δ*hdcr* tomograms. Slice thickness: 7 nm.
908
909 **Extended Data Fig. 9. Overview of HDCR subtomogram averaging, and helical pitch**
910 **comparison between *in vitro* and *in situ* structures. a**, Processing flowchart used for HDCR
911 subtomogram averaging *in situ*. For additional details, see Methods. **b**, Fourier shell correlation
912 (FSC) curves from the final subtomogram average (displayed in Fig. 5G). **c**, comparison of
913 observed helical pitch *in vitro* (98.5 nm with rise: 68.4 Å, twist: 25°) and *in situ* (289.5 nm with
914 rise: 67.8 Å, twist: 8.43°).
915
916 **Extended Data Table 1. Cryo- EM data collection, refinement and validation statistics.**
917
918

a

HydA2
HycB4$_2$
HycB4$_1$
159 Å
188 Å
90°
HycB4$_2$
HydA2
HycB4$_1$
HycB4$_2$
HycB3
FdhF
150 Å
90°
FdhF
HycB3
HycB4$_1$
HycB4$_2$
HydA2

b

HydA2
HycB4$_2$
HycB4$_1$
90°
HydA2
HydA2
HycB4$_2$
HycB4$_1$
HycB4$_2$
HycB3
FdhF
90°
FdhF
HycB3
HycB4$_1$
HycB4$_2$
HydA2

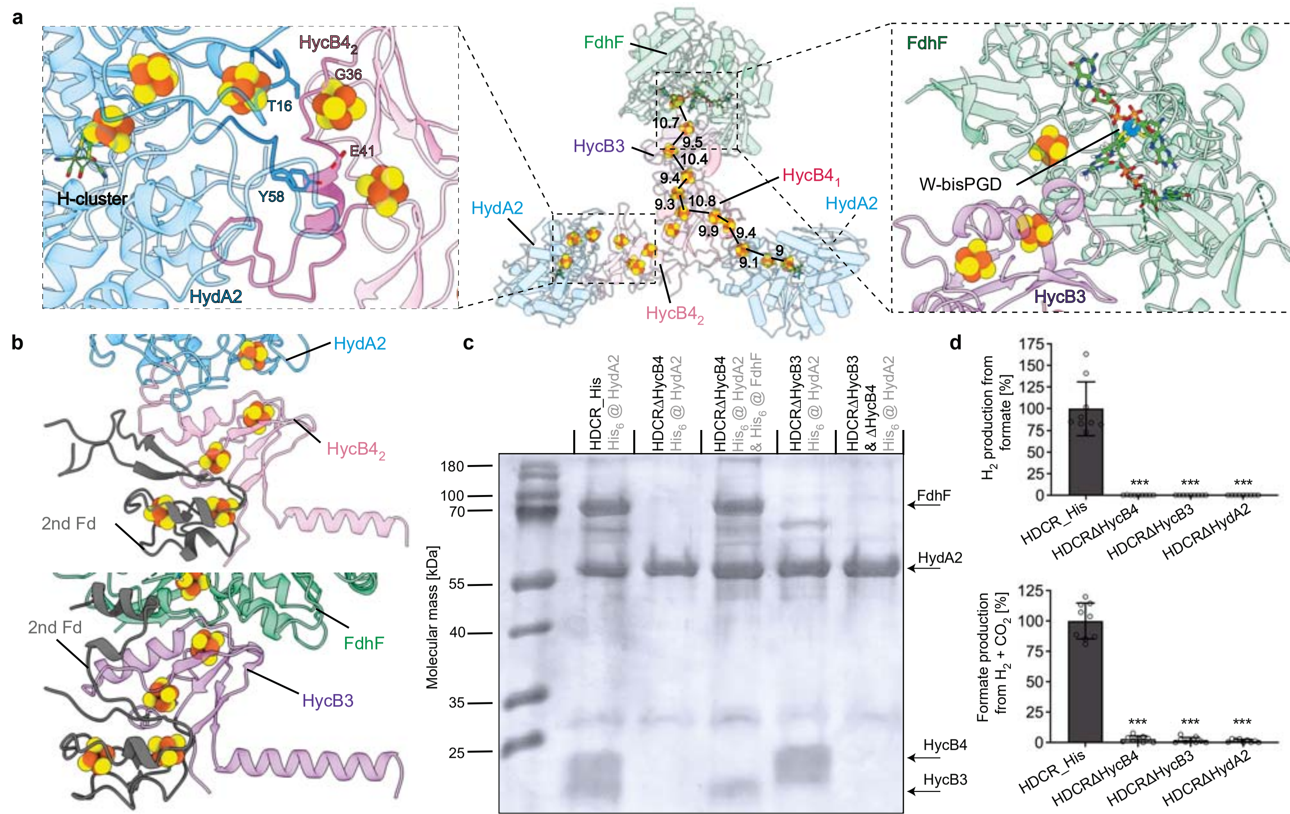

a
HycB4$_2$
G36
T16
E41
H-cluster
Y58
HydA2
FdhF
HycB3
10.7
9.5
10.4
9.4
HycB4$_1$
9.3
10.8
9.9
9.4
9
9.1
HydA2
HydA2
HycB4$_2$
FdhF
W-bisPGD
HycB3
b
HydA2
HycB4$_2$
2nd Fd
2nd Fd
FdhF
HycB3
c
HDCR_His
His$_6$ @ HydA2
HDCRΔHycB4
His$_6$ @ HydA2
HDCRΔHycB4
His$_6$ @ HydA2
& His$_6$ @ FdhF
HDCRΔHycB3
His$_6$ @ HydA2
HDCRΔHycB3
& ΔHycB4
His$_6$ @ HydA2
Molecular mass [kDa]
180
100
70
55
40
35
25
FdhF
HydA2
HycB4
HycB3
d
H_2 production from formate [%]
175
150
125
100
75
50
25
0
***
***
***
HDCR_His
HDCRΔHycB4
HDCRΔHycB3
HDCRΔHydA2
Formate production from H_2 + CO_2 [%]
125
100
75
50
25
0
***
***
***
HDCR_His
HDCRΔHycB4
HDCRΔHycB3
HDCRΔHydA2

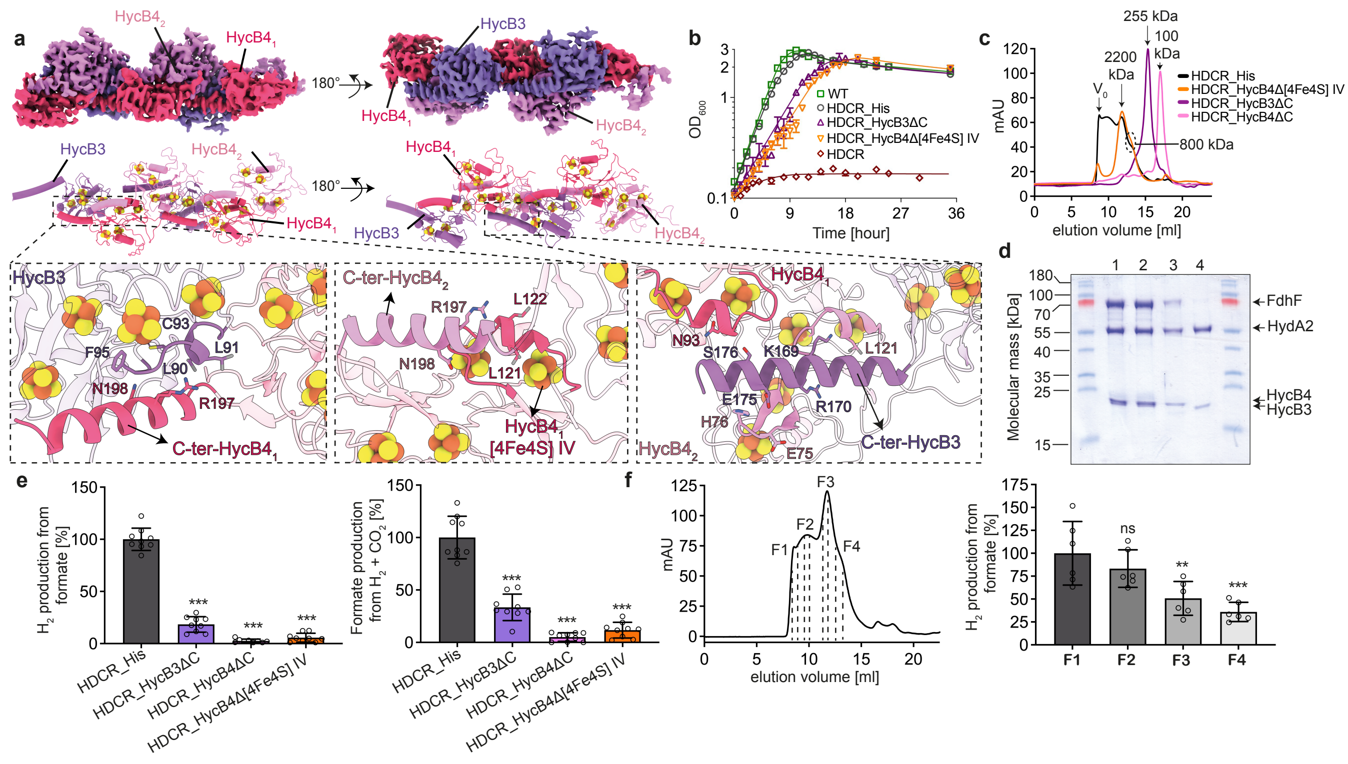
a
HycB4₂
HycB4₁
HycB3
180°
HycB4₁
HycB4₂
HycB3
HycB4₂
HycB4₁
180°
HycB4₁
HycB3
HycB4₂
HycB3
C93
F95
L91
L90
N198
R197
C-ter-HycB4₁
C-ter-HycB4₂
R197
L122
N198
L121
HycB4₁ [4Fe4S] IV
HycB4₁
N93
S176
K169
L121
E175
R170
H76
HycB4₂
E75
C-ter-HycB3
b
OD600
Time [hour]
WT
HDCR_His
HDCR_HycB3ΔC
HDCR_HycB4Δ[4Fe4S] IV
HDCR
c
255 kDa
100 kDa
2200 kDa
V0
800 kDa
mAU
elution volume [ml]
HDCR_His
HDCR_HycB4Δ[4Fe4S] IV
HDCR_HycB3ΔC
HDCR_HycB4ΔC
d
Molecular mass [kDa]
FdhF
HydA2
HycB4
HycB3
e
H2 production from formate [%]
Formate production from H2 + CO2 [%]
HDCR_His
HDCR_HycB3ΔC
HDCR_HycB4ΔC
HDCR_HycB4Δ[4Fe4S] IV
***
f
mAU
elution volume [ml]
F1
F2
F3
F4
H2 production from formate [%]
ns
**
***

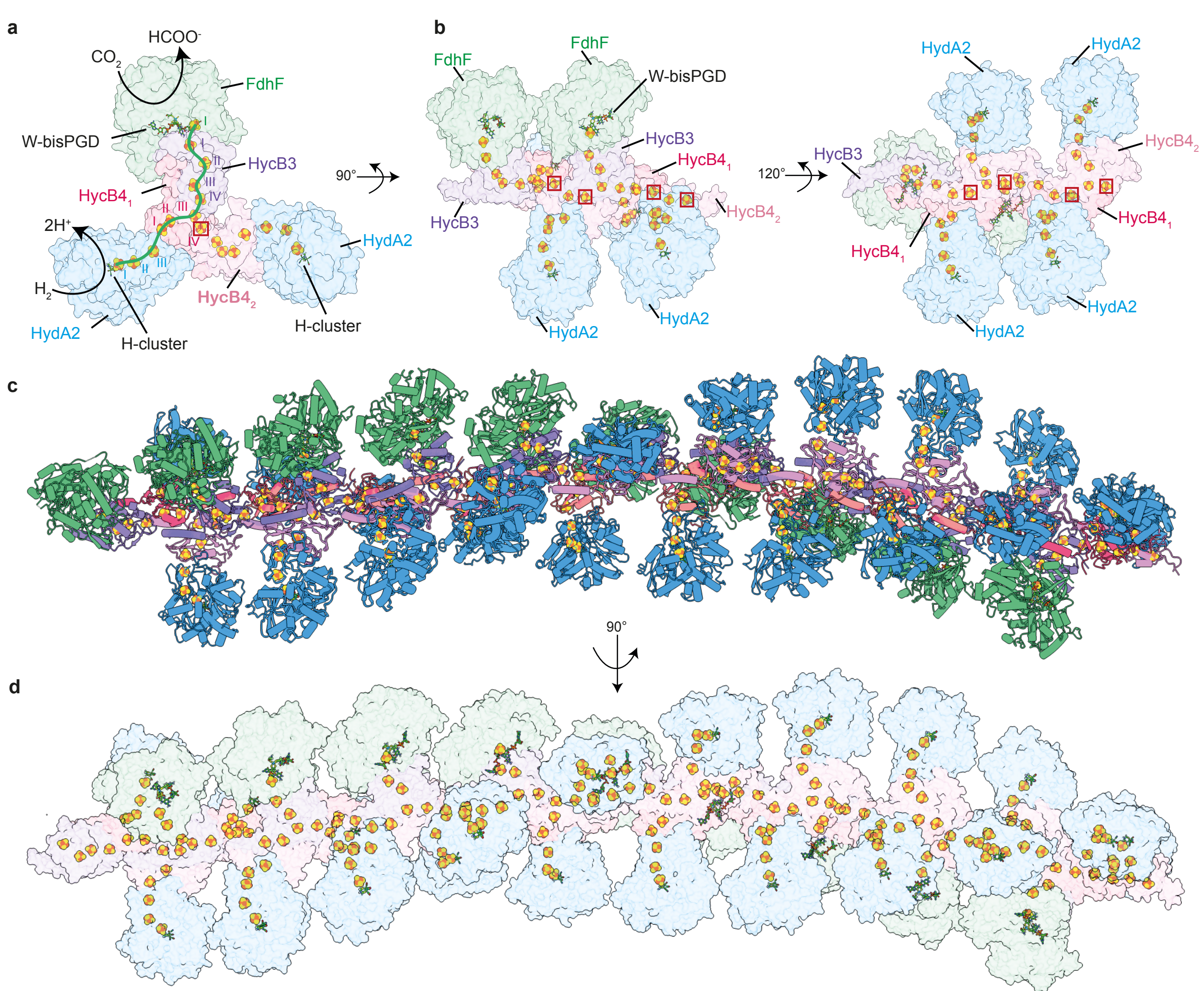
a
HCOO-
CO2
FdhF
W-bisPGD
HycB3
HycB41
2H+
H2
HycB42
HydA2
HydA2
H-cluster
H-cluster
90°
b
FdhF
FdhF
W-bisPGD
HycB3
HycB41
HycB3
HycB42
HydA2
HydA2
120°
HydA2
HydA2
HycB3
HycB42
HycB41
HycB41
HydA2
HydA2
c
90°
d

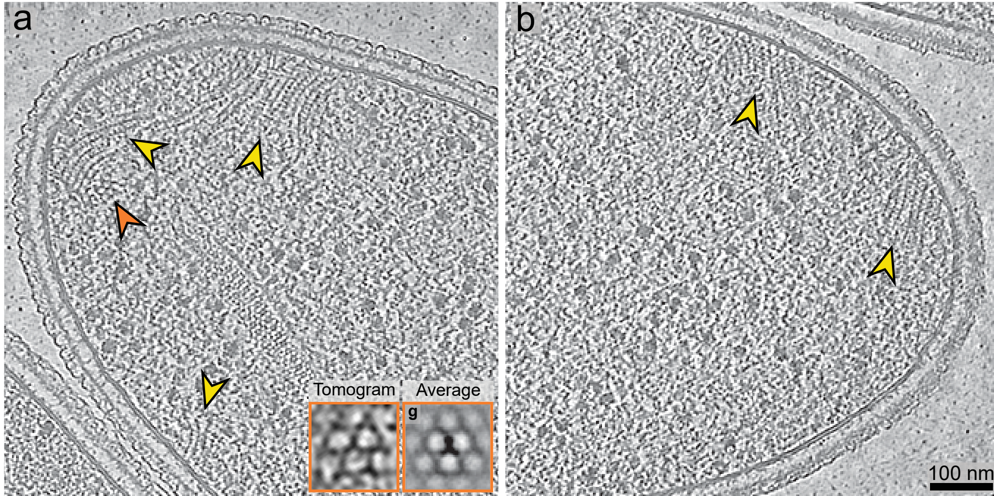
a
b
Tomogram
Average
g
100 nm

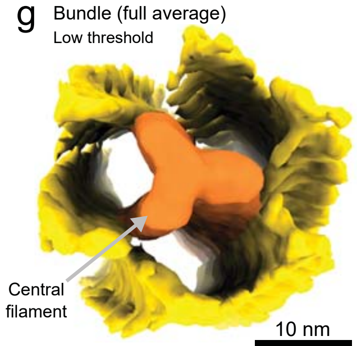
g
Bundle (full average)
Low threshold
Central filament
10 nm

h
Full model
Low threshold

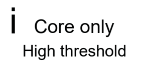
i
Core only
High threshold

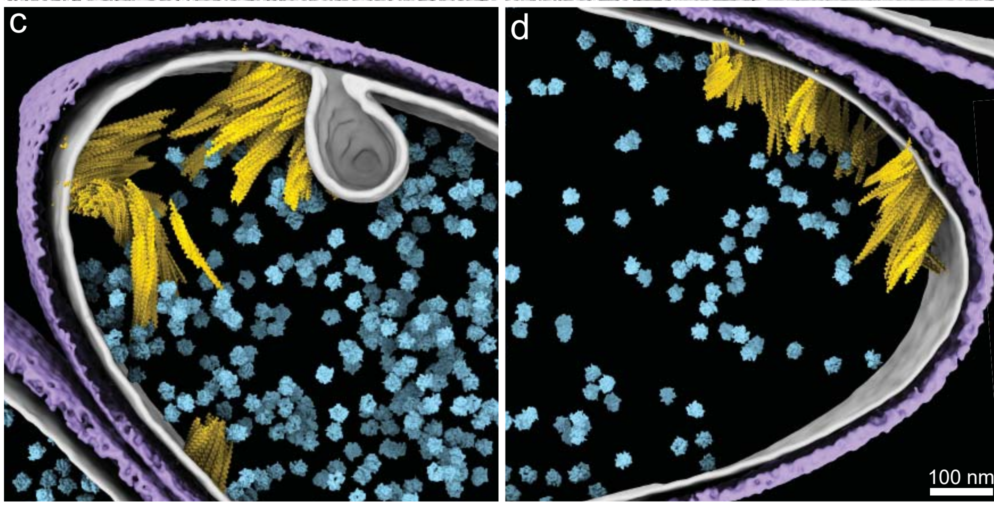
c
d
100 nm

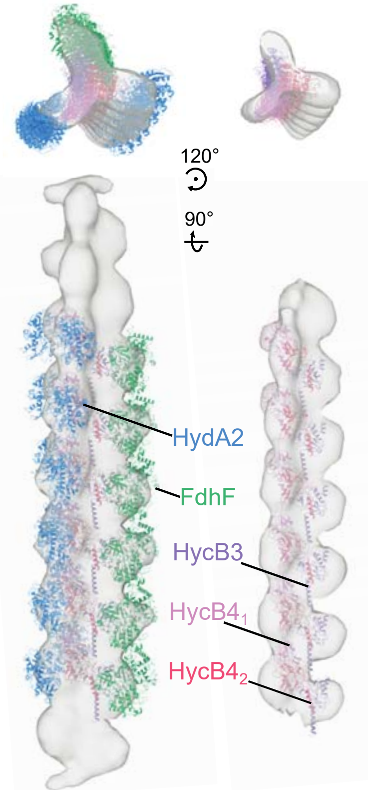
120°
90°
HydA2
FdhF
HycB3
HycB4$_1$
HycB4$_2$

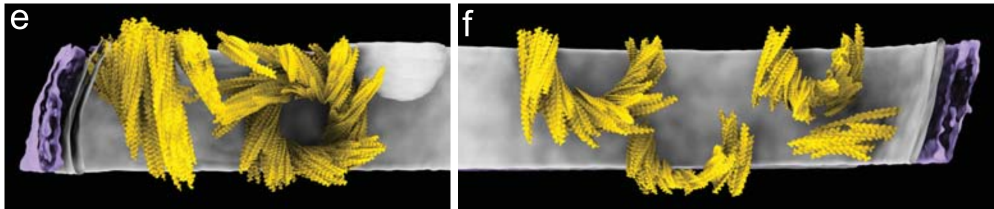
e
f